Temperature dependent Raman linewidths in transition metal dichalcogenides

G. P. Srivastava and Iorwerth O. Thomas

School of Physics, University of Exeter,

Stocker Road, Exeter EX4 4QL, United Kingdom

(Dated: July 2, 2018)

Abstract

Using a semi-*ab-initio* theoretical method we examine the temperature dependent linewidth of the Raman modes in bulk and monolayer transition metal dichalcogenides (TMDs) MoS_2, WS_2 and $MoTe_2$. It is found that different Raman modes show different linewidths and different temperature dependences with respect to each other for a given sample and across different TMDs. We explain these characteristics as arising from a combination of phonon density of states, Raman mode frequency, and the relative contributions of temperature-independent mass-defect scattering and temperature-dependent intrinsic anharmonic interactions. Reported measurements for samples prepared under experimental conditions have been explained by adding frequency-dependent inhomogeneity-related background contribution to our theoretical results for the pure and homogeneous samples.

PACS numbers: 63.20.dk, 63.22.-m,78.30.-j

I. INTRODUCTION

Monolayer and few-layer transition metal dichalcogenides (TMDs) in their 2H MX_2 phases (M=Mo and W and X=S, Se and Te) are considered to be possible alternative components to graphene within superior thermal and opto-electronic devices. Due to its low thermal conductivity, finite band gap and high electron mobility, monolayer MoS_2 would be a superior component material for thermoelectric [1] and opto-electronic devices [2–4]. Thin flakes of WS_2 show similar promise for electronic device applications [5]. Raman spectroscopy has been employed to investigate the zone-centre phonon properties of atomically thin MX_2 TMDs. In particular, Raman spectroscopy has been used to identify the number of atomic layers in thin flakes of TMDs [6–8]. The Raman peaks of a material possess a temperature dependent width. Accurate determination of the widths of these peaks and their behaviour with temperature is of fundamental and practical importance to the characterisation of that material. Although there are several measurements of the two highest (A and E) Raman peaks in TMDs [9–13], the vast majority of studies report measurements at a single temperature only, with a few exceptions such as Sahoo *et al*'s [14] report of the variation of the highest A mode in a few-layer MoS_2 sample in the temperature range 83-523 K. In both monolayer and bulk MoS_2, the highest A mode is found to be wider than the highest E mode [9–13]. The measurements made by Sahoo *et al* [14] show that for a high-purity few-layer MoS_2 the linewidths of the highest A and E modes increase non-linearly when the sample temperature increases from 100 K to 500 K. In contrast, a CVD grown monolayer sample of MoS_2 is reported to show a very weak temperature variation [11].

In this work we examine which physical parameters determine the width and temperature variation of Raman-active modes in bulk and monolayer MX_2 TMDs with different choices of cation and anion. To do this, we employ a semi-*ab-initio* theoretical method to calculate the temperature dependent linewidths of the Raman modes in bulk and monolayer TMDs MoS_2, WS_2 and $MoTe_2$. It is found that in pure and homogeneous samples different in-plane E and out-of-plane A modes show different linewidths and different temperature dependences with respect to each other for a given sample and across different TMDs. We explain these as arising from a combination of mode frequency location, phonon dispersion relations, temperature-independent isotopic mass-defect scattering, and intrinsic anharmonic interactions of the modes. We further explain reported temperature variations

of the highest frequency A and E modes in bulk and monolayer MoS_2 experimental samples through the addition to our theory of a frequency dependent background contribution accounting for the inhomogeneities present in actually existing materials.

II. THEORY

For a pure and homogeneous sample of size larger than the intrinsic phonon mean free path we express the linewidth of a Raman phonon mode of frequency $\omega_{\boldsymbol{q}_0 s}$ with wavevector $\boldsymbol{q}_0 = \boldsymbol{0}$ and polarisation s in terms of its full-width at half maximum FWHM($\boldsymbol{q}_0 s$) as [15]

$$\text{FWHM}(\boldsymbol{q}_0 s)|_{\text{ideal sample}} = \hbar\tau^{-1}_{\boldsymbol{q}_0 s} = \hbar[\tau^{-1}_{\boldsymbol{q}_0 s}(\text{md}) + \tau^{-1}_{\boldsymbol{q}_0 s}(\text{anh})], \tag{1}$$

where the two terms on the right hand side are contributed by mass defect and anharmonic scattering events respectively. For pure and homogeneous samples we consider mass defect scattering to be due to isotopic mass defects, *i.e.* we express $\tau^{-1}_{\boldsymbol{q}s}(\text{md})$ as $\tau^{-1}_{\boldsymbol{q}s}(\text{isotopic md})$ using the expression [16]

$$\tau^{-1}_{\boldsymbol{q}s}(\text{isotopic md}) = \frac{\pi}{2N_0}\omega^2_{\boldsymbol{q}s}\sum_{\boldsymbol{q}'s'}\delta(\omega_{\boldsymbol{q}s} - \omega_{\boldsymbol{q}'s'})\sum_{\boldsymbol{b}}\Gamma(\boldsymbol{b})|\boldsymbol{e}^{\star}_{\boldsymbol{q}s}(\boldsymbol{b})\cdot\boldsymbol{e}_{\boldsymbol{q}'s'}(\boldsymbol{b})|^2, \tag{2}$$

where $\boldsymbol{b}$ labels isotopic atomic sites in the unit cell, $\boldsymbol{e}_{\boldsymbol{q}s}(\boldsymbol{b})$ is an eigenvector of the lattice dynamical matrix, and the mass disorder coefficient is $\Gamma(\boldsymbol{b}) = \sum_i f_i(\boldsymbol{b})(1 - M_i(\boldsymbol{b})/\bar{M}(\boldsymbol{b}))^2$ with $\bar{M}(\boldsymbol{b})$ being the average mass of the b$^{\text{th}}$ atom and $f_i(\boldsymbol{b})$ being the frequency weighting of the i^{th} isotope with mass $M_i(\boldsymbol{b})$. We evaluate the anharmonic contribution using the semi-*ab-initio* scheme described in [16] to calculate the three phonon scattering rates:

$$\begin{aligned}
\tau^{-1}_{3\text{ph},\boldsymbol{q}s} &= \frac{\pi\hbar}{\varrho N_0\Omega}\frac{\bar{\gamma}^2(T)}{\bar{c}^2}\sum_{\boldsymbol{q}'s',\,\boldsymbol{q}''s'',\,\boldsymbol{G}}\omega\omega'\omega''\delta_{\boldsymbol{q}+\boldsymbol{q}'+\boldsymbol{q}'',\boldsymbol{G}} \\
&\times \Big[\frac{\bar{n}'(\bar{n}''+1)}{(\bar{n}+1)}\delta(\omega+\omega'-\omega'') + \frac{1}{2}\frac{\bar{n}'\bar{n}''}{\bar{n}}\delta(\omega-\omega'-\omega'')\Big], \\
&= \frac{\pi\hbar}{2\varrho N_0\Omega}\frac{\bar{\gamma}^2(T)}{\bar{c}^2}\sum_{\boldsymbol{q}'s',\,\boldsymbol{q}''s'',\,\boldsymbol{G}}\omega\omega'\omega''\delta_{\boldsymbol{q}+\boldsymbol{q}'+\boldsymbol{q}'',\boldsymbol{G}} \\
&\times \Big[2(\bar{n}'-\bar{n}'')\delta(\omega+\omega'-\omega'') + (1+\bar{n}'+\bar{n}'')\delta(\omega-\omega'-\omega'')\Big],
\end{aligned} \tag{3}$$

where ϱ is the mass density, $\bar{c}^2$ is the average acoustic velocity, $\bar{\gamma}^2(T)$ is the square of a temperature dependent Grüneisen parameter, $\bar{n}, \bar{n}', \bar{n}''$ are Bose-Einstein distribution functions for phonons with frequencies $\omega, \omega', \omega''$, and $\boldsymbol{G}$ is a reciprocal lattice vector. The alternative expressions in the above equation are related via the identities $\bar{n}'(\bar{n}''+1)/(\bar{n}+1) = \bar{n}' - \bar{n}''$

and $\bar{n}'\bar{n}''/\bar{n} = 1 + \bar{n}' + \bar{n}''$. The square of the temperature-dependent but mode-independent Grüneisen constant is computed within the quasi-harmonic approximation as follows [17–20]:

$$\bar{\gamma}^2(T) = \frac{\sum_{\boldsymbol{q}s} \gamma^2_{\boldsymbol{q}s} \omega^2(\boldsymbol{q}s) \bar{n}(\boldsymbol{q}s)(\bar{n}(\boldsymbol{q}s)+1)}{\sum_{\boldsymbol{q}s} \omega^2(\boldsymbol{q}s) \bar{n}(\boldsymbol{q}s)(\bar{n}(\boldsymbol{q}s)+1)}. \tag{4}$$

Phonon eigensolutions (frequencies and atomic displacement vectors) were computed using the ab-initio DFPT (density functional perturbation theory) package Quantum Espresso with PBE pseudopotentials [21] on Monkhorst-Pack grids [22] of $45 \times 45 \times 1$ for monolayer and $28 \times 28 \times 7$ for bulk systems.

Samples prepared under experimental conditions are inherently inhomogeneous and contain varying concentrations of defects of different kinds. The measurement accuracy of Raman linewidths is affected by the resolution capability of the experimental apparatus. These effects may be accounted for through the inclusion of a temperature-independent but frequency-dependent background contribution to the theoretical linewidth contribution expressed in Eq. (1) (as in [14]):

$$\mathrm{FWHM}(\omega_{\mathbf{0}s})|_{\text{real sample}} = \mathrm{FWHM}(\omega_{\mathbf{0}s})|_{\text{background}} + \mathrm{FWHM}(\omega_{\mathbf{0}s})|_{\text{ideal sample}}, \tag{5}$$

where $\mathrm{FWHM}(\omega_{\mathbf{0}s})|_{\text{background}}$ is the background contribution for the linewidth of the Raman mode of frequency $\omega_{\mathbf{0}}$ and polarisation s. The background contribution due to the rippling or roughness usually present in real 2D materials would probably become more important as temperature is reduced. In the present study we are not able to include such a contribution explicitly, and therefore confine our discussion to perfectly flat 2D situation. Raman linewidths in doped TMDs will also include contributions from the electron-phonon interaction. However, in real TMD systems the electron-phonon contribution will be overshadowed by the large inhomegeneity driven background contribution in the temperature range of study in this work. Therefore we have not included any contribution from electron-phonon interaction.

III. RESULTS

Eigenmodes of the Raman atomic vibrations at the Brillouin zone centre for 2H bulk (point group D_{6h}) and monolayer (point group D_{3h}) TMDs are presented in Fig. 1. The 1D (A and B) and 2D (E) labellings of the modes are decomposed from the zone centre

representation as

$$\begin{aligned}\Gamma_{\rm optical}(\text{2H bulk}) &= A_{1g}(\text{R}) + A_{2u}(\text{IR}) + B_{1u}(\text{IN}) + B^1_{2g}(\text{IN}) + B^2_{2g}(\text{IN}) \\ &\quad + E_{1u}(\text{IR}) + E_{1g}(\text{R}) + E_{2u}(\text{IN}) + E^2_{2g}(\text{R}) + E^1_{2g}(\text{R}) \\ \Gamma_{\rm optical}(\text{monolayer}) &= A_1^{'}(\text{R}) + A_2^{''}(\text{IR}) + E^{'}(\text{R}+\text{IR}) + E^{''}(\text{R}), \end{aligned} \tag{6}$$

with R, IR and IN indicating Raman, infrared and inactive modes, respectively. Due to symmetry reduction as the number of layers is reduced, the bulk modes A_{1g} and B_{1u} become the monolayer A_1' mode, the bulk modes E_{1u} and E^1_{2g} become the monolayer E' mode, and the bulk modes E_{1g} and E_{2u} become the monolayer E'' mode. The Raman active modes appear in the following decreasing order of frequency: $A_{1g}, E^1_{2g}, E_{1g}, E^2_{2g}$ for bulk MoS_2 and WS_2; $E^1_{2g}, A_{1g}, E_{1g}, E^2_{2g}$ for bulk $MoTe_2$; A_1', E', E'' for monolayer MoS_2 and WS_2; and E', A_1', E'' for monolayer $MoTe_2$.

From Eq. (2) it is clear that the mass defect scattering of a Raman mode is governed by the product of three terms: the strength of mass-defect $|\Delta M/\bar{M}|^2$, the square of the frequency of the mode $\omega^2_{\mathbf{0}s}$ and the density of states at the mode frequency $DOS(\omega_{\mathbf{0}s})$. Frequency of occurence and masses of stable isotopes for Mo, W, S and Te are presented in Tab. I. Note that the factor $|\Delta M/\bar{M}|$ is approximately 3%, 8%, 8% and 13% for W, Mo, Te and S, respectively. Figure 2 shows the phonon density of states and the frequency locations of the Raman modes for the three TMDs studied here.

As can be seen from Eq. (3), the anharmonic scattering at temperature T of a phonon of frequency ω is usually a complicated function $f(\omega, T)$. With a change in temperature there will be a slight change in the phononic gaps in the phonon spectra presented in Fig. 2. Such changes are expected to have a minimal effect on the acoustic-optical phonon interaction. While in our numerical calculations of the linewidths we evaluate the full expression in Eq. (3), including the mode-averaged, temperature dependent Grüneisen constant results published in our previous papers [16, 26], a simplified description is that at a given temperature the anharmonic scattering of a Raman mode is determined from $\omega^2_{\mathbf{0}s} \times JDOS(\omega_{\mathbf{0}s})$, with the joint density of states $JDOS(\omega_{\mathbf{0}s})$ of the $\omega_{\mathbf{0}s}$ mode with two other modes being subject to appropriate momentum conservation conditions. The description of the two terms in Eq. (3) is similar to that employed in discussion of optical and electronic properties (see, e.g. [24, 25]). Crudely speaking, the $JDOS(\omega_{\mathbf{0}s})$ is a measure of the product of the density of states at $\omega_{\mathbf{0}s}$ and at the other two frequencies with which this mode partakes in allowed three-phonon

events. While processes both in term 1 (class 1 or coalescence) and term 2 (class 2 or decay) of Eq. (3) contribute to the anharmonic lifetime of a phonon mode, it is the latter (decay) term that generates the dominant contribution for the highest Raman mode. Traditionally this contribution has been explained using a number of decay channels involving acoustic (ac) and optical (op) branches, notably the Klemens channel [27]: op $\rightarrow$ ac + ac, the Ridley channel [28]: op $\rightarrow$ op + ac, the Vallèe-Bogani channel [29]: op $\rightarrow$ op(same branch) + ac, and the Barman-Srivastava channel [30]: op $\rightarrow$ op + op. While it would be appropriate to analyse the the lifetime of the highest bulk Raman mode A_{1g} (or the highest monolayer mode A') in MoS_2 and WS_2 in terms of these decay channels, it would not be entirely so for the A_{1g} (or A') mode in $MoTe_2$ as this mode can partake in both coalescence and decay events due to its positioning in the frequency spectrum.

A. Results for systems with ideal structures

Figure 3 presents our computed results for the linewidths of Raman active modes in ideal (*i.e.* defect free and homogeneous) bulk and monolayer TMDs MoS_2, WS_2 and $MoTe_2$ in the temperature range 50-500 K. Considering the two contributions in Eq. (1) temperature variation of the linewidth of each Raman mode can be expressed as

$$\begin{aligned} \text{FWHM}|_{\text{ideal sample}} &= \text{FWHM}|_{\text{md}} + \text{FWHM}|_{\text{anh}} \\ &= \alpha_{\text{md}} + \beta_0 + \beta(T), \end{aligned} \tag{7}$$

where $\alpha_{\text{isotopic md}}$ is a temperature-independent isotopic mass defect contribution, β_0 is the temperature-independent contribution due to spontaneous anharmonic decay, and $\beta(T)$ is the temperature-dependent anharmonic contribution at temperature T. We note that β_0 is the first of the three contributions in the second term in Eq. (3). Table II lists the temperature-independent linewidth contributions α_{md} and β_0 in these systems. We note that both α_{md} and β_0 contribute nothing to the overall linewidth of the E^2_{2g} mode in all of the three bulk TMDs studied here. Also, β_0 contributes nothing to the overall linewidth of the E'' mode in all of the three ML TMDs studied here.

We make several observations from the results presented in Fig. 3. (i) The first observation is that, consistent with the discussion presented in the previous paragraph, linewidths do not necessarily exhibit the same temperature dependence either across different modes of

the same system or for a chosen mode across all systems. However, for bulk samples rather similar temperature variation is noted for the A_{1g}, E^1_{2g} and E_{1g} modes in MoS_2, for the A_{1g} and E_{1g} modes in WS_2, for the A_{1g} and E^1_{2g} modes in $MoTe_2$. For monolayer systems, rather similar linewidth temperature variation is noted for all Raman active modes in all of the three TMDs. (ii) The second observation is that there is no firm trend in the linewidth of modes with regards to their frequency location either for a given system or across the TMDs studied. Above 200 K, the A_{1g} mode is widest for bulk MoS_2 and WS_2, while the E^1_{2g} mode is the widest for bulk $MoTe_2$. The A'_1 mode is the widest for ML MoS_2, the E' mode is the widest for ML WS_2 and ML $MoTe_2$. The bulk E_{1g} is usually sharper than the E^1_{2g} mode (except above 400 K for WS_2), and the E^2_{2g} mode is the sharpest of all. For ML systems the E'' mode is the sharpest of all. (iii) The third observation refers to the relative widths of the highest lying Raman mode in the TMDs studied here. In the temperature range of the present study, the bulk E^1_{2g} mode in $MoTe_2$ is wider above 300 K than the A_{1g} mode in MoS_2, which in turn is wider than the A_{1g} mode in WS_2. The ML A'_1 mode in MoS_2 is wider than the E' mode in $MoTe_2$, which in turn is wider than the E' mode in WS_2. (iv) The fourth observation is that the monolayer Raman modes show much less pronounced temperature dependence than the corresponding bulk modes.

We first discuss the results for the Raman modes with the top two frequencies. The two highest Raman modes,*viz.* A_{1g} (A'_1) and E^1_{2g} (E'), in MoS_2 show reasonably similar temperature variation, with their relative widths being in accord with the mass defect contribution increasing with their frequency locations (*cf.* Tab. II). In WS_2, the lower frequency mode E^1_{2g} has a higher density of states and so undergoes stronger mass defect scattering than the higher frequency mode A_{1g}. As a result it has a slightly wider linewidth compared to the A_{1g} mode below 100 K. It also has a much weaker dependence on temperature. The much slower temperature variation of the A'_1 mode for monolayer WS_2 and monolayer $MoTe_2$ indicates a dominant mass-defect contribution. The relatively stronger temperature variation for monolayer MoS_2 indicates that the strength of the anharmonic scattering is more pronounced in this system than in the other two systems. Compared to A'_1, the A_{1g} mode in all three bulk materials becomes wider and shows a sharper rise with temperature. This is because the anharmonic contribution increases since there are more allowed three-phonon combinations in the bulk structure, which has twice as many phonon branches.

The E^1_{2g} (E') and A_{1g} (A'_1) modes in $MoTe_2$ have have swapped their frequency ordering.

The mass defect scattering rate of the E^1_{2g} (E') mode is much stronger than that of the A_{1g} (A'_1) mode (*cf.* see Tab. II). As can be seen from the temperature variation, the anharmonic decay rate contribution to the lifetime of the A_{1g} (A'_1) mode is similar to the sum of the coalescent and decay rate contributions to the lifetime of the E^1_{2g} (E') mode. Consequently, the total FWHM is wider for the latter mode.

We note that while the A_{1g} (A'_1) mode in $MoTe_2$ can partake in both coalescent and decaying three-phonon processes, the role of coalescent processes is rather insignificant in MoS_2 and WS_2. The FWHM of the A_{1g} mode of $MoTe_2$ becoming greater than that of MoS_2 above 300 K is a result of the increase in the contribution from the coalescent three-phonon processes in the former case as the temperature increases. We also note that the decay of the A_{1g} mode in MoS_2 and WS_2 takes place with significant contributions via the Klemens channel [27] (into two acoustic modes), the Ridley channel [28] (into one acoustic and one of several optical modes) and the Barman-Srivastava channel [30] (into two of several optical modes). In contrast, the decay of this mode in $MoTe_2$ via the Ridley channel and the Barman-Srivastava channel involves only low-lying optical modes.

The in-plane mode E_{1g} cannot be observed in back-geometry experiments [14]. We find that the low-frequency bulk E_{1g} and monolayer E'' modes lie in a region where the phonon density of states is low. Anharmonic scattering (contributed by both coalescence and decay processes) thus competes with mass-defect scattering. Temperature variation of the linewidth of this mode is less pronounced in $MoTe_2$ than in MoS_2 and WS_2. The E^2_{2g} bulk Raman mode undergoes the weakest mass-defect scattering because this is the lowest-frequency Raman mode lying on the low-frequency tail of the phonon density of states (*cf.* Eq. (2) and Fig. 2). It also encounters the weakest form of three-phonon scattering, as this low-frequency mode can only take part in a limited number of coalescent and decay processes. In particular, it can only decay into low-density regimes of acoustic modes. Weak temperature variation of the results in Figs. 4 indicates that mass-defect is dominant over the anharmonic contribution in controlling the linewidth of this mode.

B. Comparison of results for laboratory produced samples

Our theoretical findings for the relative widths of the A'_1, A_{1g}, E' and E^1_{2g} modes in defect-free crystalline bulk and monolayer TMDs are consistent with the reported experi-

mental measurements for MoS_2 [9–13], for WS_2 [8], and for $MoTe_2$ [31]. Also, our predicted results for low frequency Raman modes in the three TMDs are consistent with the experimental investigation of MoS_2 by Puretzky *et al* [32]. However the comparison of theoretical calculations of the temperature dependent line-width with experimental values requires that we consider the effects of sample quality, which we attempt below.

In Fig. 4 we present a comparison of our ideal sample results with published data for MoS_2 samples prepared under experimental conditions. We first note that for both bulk and monolayer systems there is a large spread in the data obtained by different groups for the bulk A_{1g}, E^1_{2g}, monolayer A'_1 and E' modes. Measured linewidths reported in Refs. [9, 11–14] are generally wider, aside from Ref. [13] which reports a sharper result than our theoretically obtained results in Fig. 3. It is notable that the difference between theoretical and experimental values is much larger for the monolayer A'_1 and E' modes.

As per Eq. (5), we attempt to reproduce experimental measurements through the addition of a frequency dependent background contribution to our theoretical results for a pure sample (as in [14]):

$$\begin{aligned} \mathrm{FWHM}|_{\text{real sample}} &= \mathrm{FWHM}|_{\text{background}} + \mathrm{FWHM}|_{\text{md}} + \mathrm{FWHM}|_{\text{anh}} \\ &= \alpha_{\text{bg}} + \alpha_{\text{md}} + \beta_0 + \beta(T), \end{aligned} \tag{8}$$

where α_{bg} is suitably chosen for the mode under consideration. As shown in Fig. 5, we obtained good reproduction of measured linewidths in MoS_2 from Sahoo *et al* [14] for the bulk A_{1g} and E^1_{2g} modes in the temperature range 150-500 K with the choices $\alpha_{\text{bg}}(A_{1g}) = 1.0$ cm^{-1}, $\alpha_{\text{bg}}(E^1_{1g}) = 1.2$ cm^{-1}. Lanzillo *et al* [11] have reported the linewidths of the monolayer A'_1 and E' modes in MoS_2 at two temperatures: 300K and 450 K. We obtained good agreement between theoretical and experimental results for their sample by making the choices $\alpha_{\text{bg}}(A'_1) = 6.2$ cm^{-1}, $\alpha_{\text{bg}}(E') = 5.82$ cm^{-1}. The choice of much larger values of the background contribution to match the experimental data of Lanzillo *et al* indicates that their sample is characterised by a high density of defects and/or a high level of inhomogeneity. Compared to bulk samples, monolayer samples prepared using presently employed experimental techniques are more likely to contain larger levels of defects and inhomogeneities. With suitable background estimates one can relate experimental measurements and theoretical calculations of the linewidths of lower frequency Raman modes for bulk and ML samples of the three TMDs studied in this work. While the predicted theoretical results in Fig. 5

are in agreement with the measured values for temperatures above 100 K, we notice that the experimental data at 100 K deviates from the prediction at 100 K. We are unable to provide a proper explanation for this, but speculate that it could be due to a local warming effect caused by the laser power used in the experimental study.

IV. SUMMARY

In summary, we have presented a detailed semi-*ab-initio* study of the temperature dependent linewidths of the Raman modes in 2H bulk and monolayer MoS_2, WS_2 and $MoTe_2$ (*i.e.* TMDs with different choices of cation and anion). It is found that different Raman modes show different linewidths and different temperature dependences with respect to each other for a given sample and across different TMDs. In general, monolayer Raman modes show weaker temperature dependence than their bulk counterparts do.

We have explained these characteristics as arising from a combination of phonon density of states, mode location in frequency spectrum, and the relative contributions of temperature-independent mass-defect scattering and temperature-dependent intrinsic anharmonic interactions. Our results for the temperature dependent variation of the linewidth of the A_{1g} mode in bulk MoS_2 are in good agreement with the experimentally measured results of Sahoo *et al* [14] for a few-layer MoS_2 sample, provided that the effect of sample inhomogeneity is included as a frequency-dependent background contribution over and above our theoretical results for ideally perfect crystalline system. We have similarly explained the width and and temperature variation of the A_1' and E' modes observed in the work of Lanzillo *et al* [11] for monolayer MoS_2.

Acknowledgements

This work has been possible with funds from the Leverhulme Trust (UK) through Grant No. RPG-2016-186, which provided financial support to IOT and purchase of computer nodes for carrying out numerical calculations. Calculations were performed on the Ceres cluster at the University of Exeter.

[1] M. Buscema *et al*, Nano Lett. **13**, 358 (2013).

[2] S. Ghatak *et al*, ACS Nano **5**, 7707 (2011).

[3] H. Wang *et al*, Nano Lett. **12**, 4674 (2012).

[4] Q. H. Wang *et al*, Nat. Nanotechnol. **7**, 699 (2012).

[5] D. Braga *et al*, Nano Lett. **12**, 5218 (2012).

[6] C. Lee *et al*, ACS Nano **4**, 2695 (2010).

[7] H. Li *et al*, Adv. Func. Mater. **22**, 1385 (2012).

[8] A. Berkdemir *et al*, Using Raman Spectroscopy. Sci. Rep. **3**, 1755 (2013).

[9] S. Najmaei *et al*, Appl. Phys. Lett. **100**, 013106 (2012).

[10] K. Gołasa *et al*, Acta Physica Polonica **124**, 849 (2013).

[11] N. A. Lanzillo *et al*, Appl. Phys. Lett. **103**, 093102 (2013).

[12] S. Mignuzzi *et al*, Phys. Rev. B **91**, 195411 (2015).

[13] H. Guo *et al*, Appl. Phys. A **122**, 375 (2016).

[14] S. Sahoo *et al*, J. Phys. Chem. **117**, 9042 (2013).

[15] L. Bergman *et al*, Phys. Rev. B **59**, 12977 (1999).

[16] I. O. Thomas and G. P. Srivastava, J. Phys. Cond. Matter. **29**, 505703 (2017).

[17] G. P. Srivastava, *The Physics of Phonons* (Taylor and Francis: New York, 1990).

[18] L. Bjerg, B. B. Iverson and G. K. Madsen, Phys. Rev B **89**, 024304 (2014).

[19] G. H. K. Madsen, A. Katre and C. Bera, Phys. Status Solidi A **215**, 802 (2016).

[20] A. Katre and G. K. H. Madsen, Phys. Rev. B **93**, 155203 (2016).

[21] P. Gianozzi *et al*, J. Phys. Cond. Mat. **21**, 395502 (2009); code available from http://www.quantum-espresso.org.

[22] H. J. Monkhorst and J. D. Pack, Phys. Rev. B **13**, 5188 (1976).

[23] K. J. R. Rosman and P. D. P. Taylor, Pure and Appl.Chem. **70**, 217 (1998).

[24] W. Y. Liang and A. R. Beal, J. Phys. C: Solid State Phys. **9**, 2823 (1976).

[25] S. K. O'Leary and S. M. Malik, J. Appl. Phys. **92**, 4276 (2002).

[26] I. O. Thomas and G. P. Srivastava, J. Appl. Phys. **123**, 135703 (2018).

[27] P. G. Klemens, Phys. Rev. **148**, 845 (1966).

[28] B. K. Ridley and R. Gupta, Phys. Rev. B **43**, 4939 (1991).

[29] F. Vallèe and F. Bogani, Phys. Rev. B **43**, 12 049 (1991).

[30] S. Barman and G. P. Srivastava, Phys. Rev. B **69**, 235208 (2004).

[31] M. Yamamoto *et al*, ACS Nano **8**, 3895 (2014).

[32] A. A. Puretzky *et al*, ACS Nano **9**, 6333 (2014).

	Isotope fraction	Isotopic mass (amu)
Mo	0.1484	91.907
	0.0925	93.905
	0.1592	94.906
	0.1668	95.905
	0.0955	96.906
	0.2413	97.905
	0.0963	99.907
W	0.0012	179.947
	0.2650	181.948
	0.1431	182.950
	0.3064	183.951
	0.2843	185.953
S	0.9493	31.972
	0.0076	32.971
	0.0429	33.968
	0.0002	35.967
Te	9.0e-4	119.904
	0.0255	121.903
	0.0089	122.904
	0.0474	123.903
	0.0707	124.904
	0.1884	125.903
	0.3174	127.904
	0.3408	129.906

TABLE I: Frequency and masses of stable isotopes for Mo, W, S, and Te, taken from Ref. [23].

	$\alpha_{\rm md}$ ($\rm cm^{-1}$)			β_0 ($\rm cm^{-1}$)		
Bulk mode	MoS_2	WS_2	$MoTe_2$	MoS_2	WS_2	$MoTe_2$
A_{1g}	1.33	0.18	0.02	0.37	0.39	0.12
E^1_{2g}	0.83	0.63	1.02	0.40	0.55	0.38
E_{1g}	0.15	0.06	0.05	0.07	0.11	0.42
E^2_{2g}	0.00	0.00	0.00	0.00	0.00	0.00
Monolayer mode	MoS_2	WS_2	$MoTe_2$	MoS_2	WS_2	$MoTe_2$
A'_1	1.58	0.40	0.04	0.07	0.02	0.00
E'	0.59	0.52	1.32	0.07	0.00	0.01
E''	0.07	0.06	0.04	0.01	0.00	0.00

TABLE II: Temperature-independent contributions $\rm FWHM_{md} \equiv \alpha_{md}$ from the isotopic mass defects and FWHM due to spontaneous anharmonic decay β_0 in bulk and monolayer TMDs.

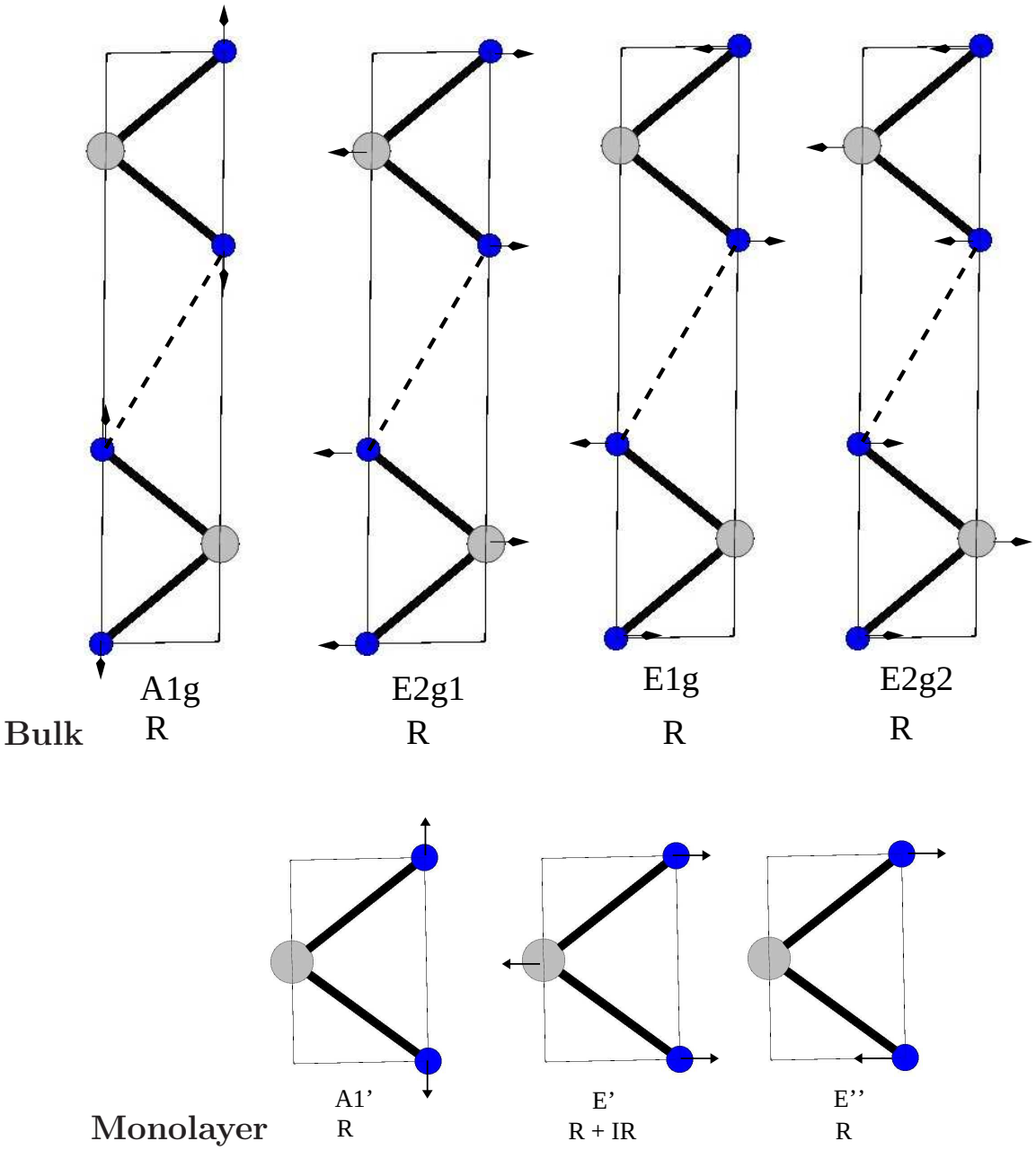

FIG. 1: Eigen atomic displacement patterns for the Raman (R) modes at the zone centre for 2H bulk and monolayer TMDs.

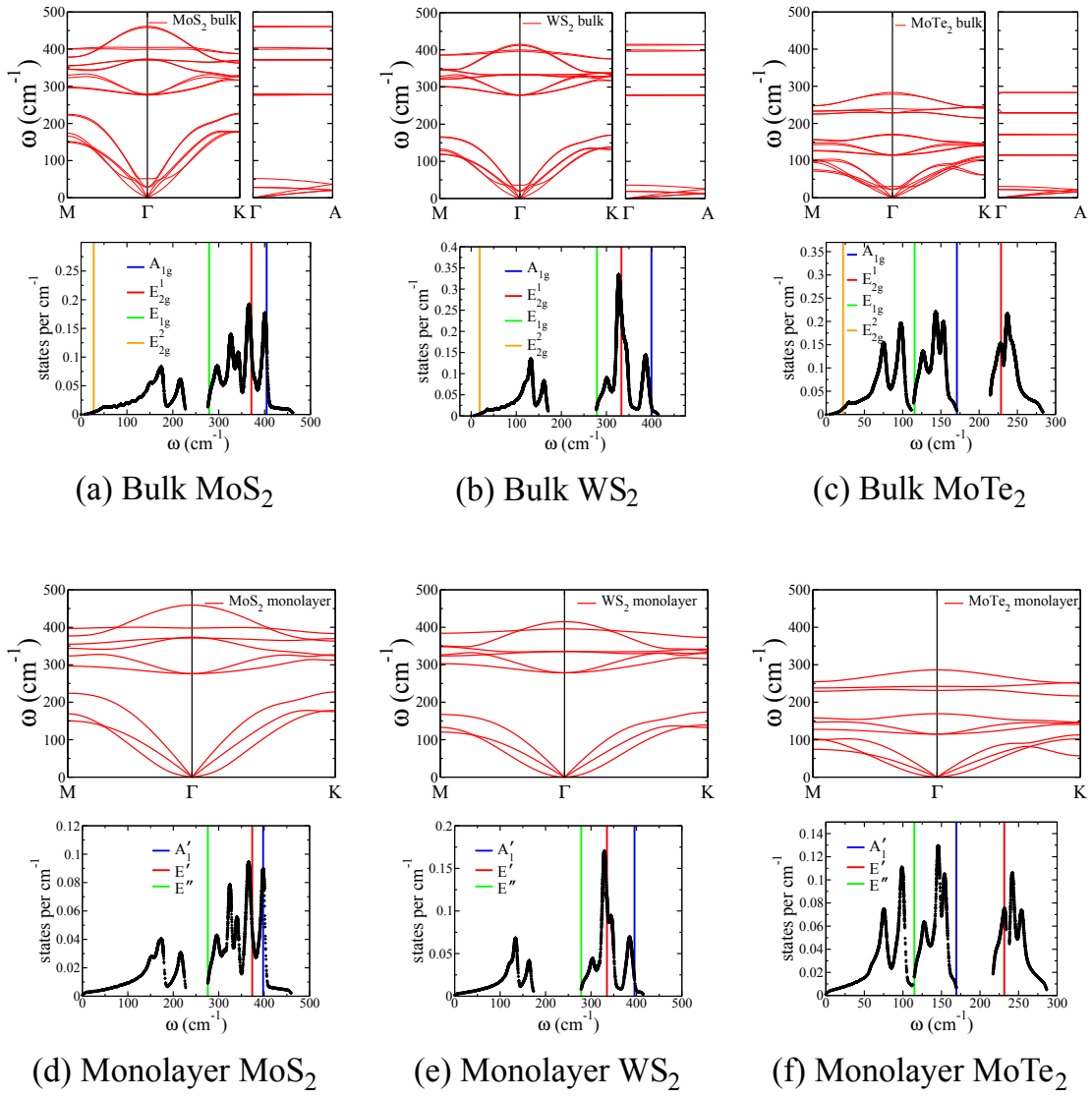

(a) Bulk MoS_2 (b) Bulk WS_2 (c) Bulk $MoTe_2$

(d) Monolayer MoS_2 (e) Monolayer WS_2 (f) Monolayer $MoTe_2$

FIG. 2: Phonon dispersion curves, phonon density of states and Raman frequencies for (a)-(c) bulk and (d)-(f) monolayer MoS_2, WS_2 and $MoTe_2$. (Phonon dispersion curves reproduced from [26], with the permission of AIP Publishing.)

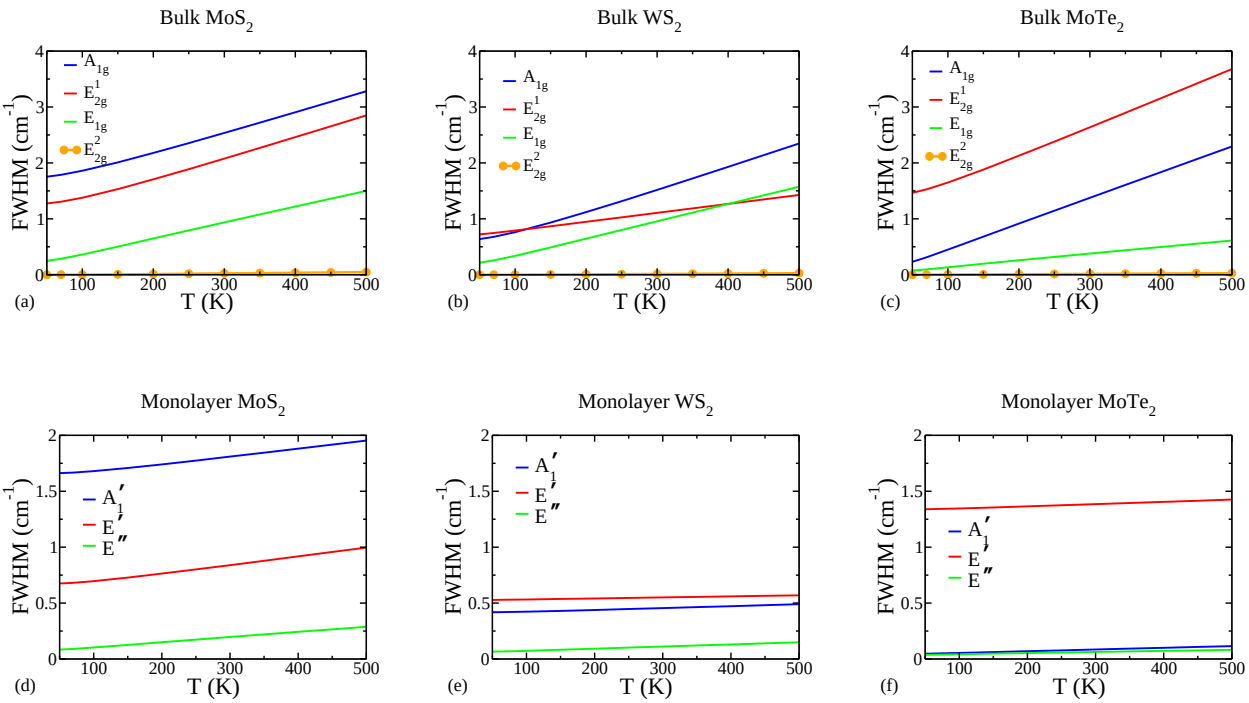

FIG. 3: Width and temperature variation of the Raman modes in defect-free and perfectly homogeneous (a)-(c) bulk and (d)-(f) monolayer TMDs.

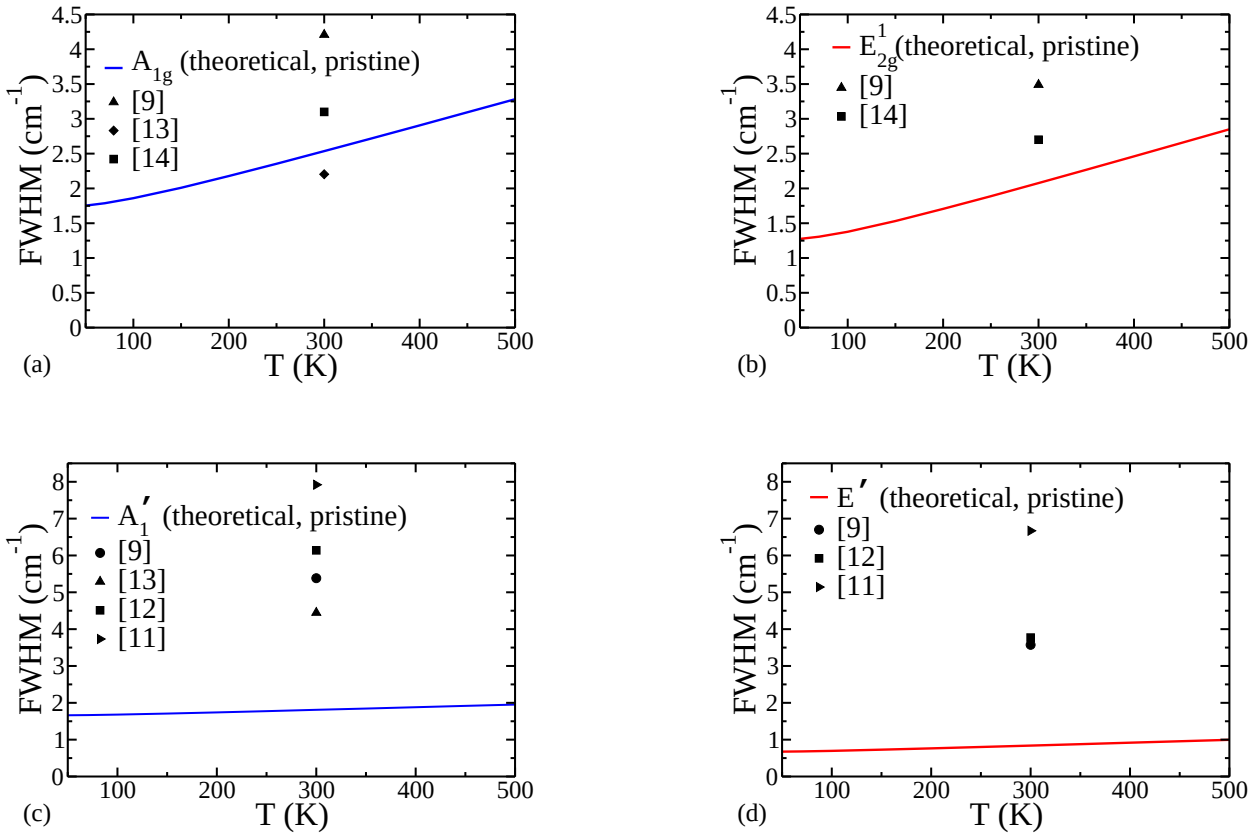

FIG. 4: Theoretical results for the temperature variation of the Raman linewidth in ideally perfect MoS_2: the (a) A_{1g} and (b) E_{2g} modes in bulk, and the (c) A_1' and (d) E' modes in monolayer. Symbols represent experimentally measured results for samples prepared under experimental conditions.

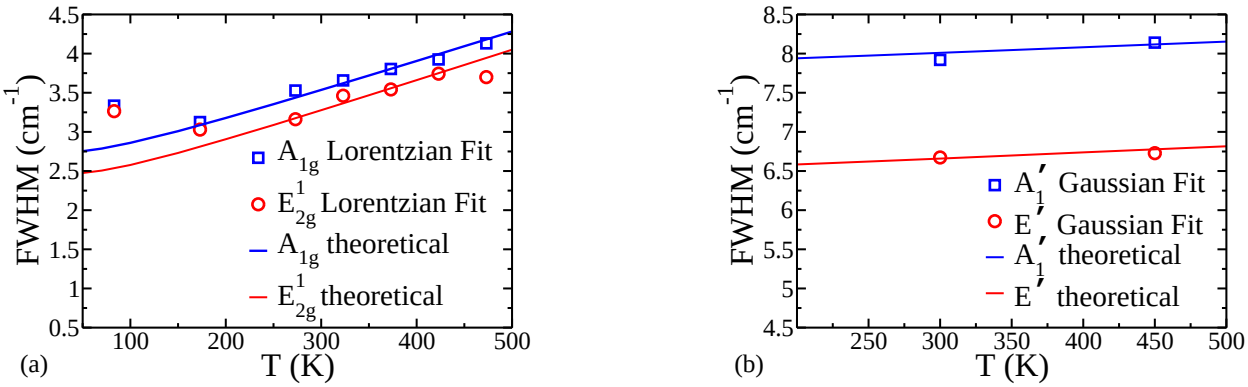

FIG. 5: Predicted width and temperature variation of Raman modes in MoS_2. Experimental linewidth results are obtained by fitting a pair of Lorentzian functions to the data in Fig. 3 (a) of [14] in the bulk case and (b) a pair of Gaussian functions to the data in Fig. 2 of [11] in the monolayer case. Note that different amounts of background contributions are added for different modes.